JPhys Photonics

PAPER • OPEN ACCESS

1 GHz fundamental repetition rate thulium-doped all-polarization maintaining modelocked fiber laser

To cite this article: C Cuadrado-Laborde *et al* 2025 *J. Phys. Photonics* **7** 015001

IOP Publishing J. Phys. Photonics 7 (2025) 015001 https://doi.org/10.1088/2515-7647/ad8d97

Journal of Physics: Photonics

OPEN ACCESS

RECEIVED
11 July 2024

REVISED
20 October 2024

ACCEPTED FOR PUBLICATION
31 October 2024

PUBLISHED
22 November 2024

PAPER

1 GHz fundamental repetition rate thulium-doped all-polarization maintaining modelocked fiber laser

C Cuadrado-Laborde[1,4,5,*], H Muñoz-Marco[2], P Pérez-Millán[2], A Díez-Cremades[1], J L Cruz[1], E Silvestre[3] and M V Andrés[1]

[1] Departamento de Física Aplicada y Electromagnetismo, ICMUV, Universidad de Valencia, C/ Dr Moliner 50, Burjassot 46100 Valencia, Spain
[2] FYLA LASER SL, Ronda Guglielmo Marconi 14, Paterna 46980, Valencia, Spain
[3] Departamento de Óptica, ICMUV, Universidad de Valencia, Dr Moliner 50, Burjassot E-46100, Spain
[4] Instituto de Física Rosario (CONICET-UNR), Blvr. 27 de Febrero 210bis, S2000EZP Rosario, Argentina
[5] Facultad de Química e Ingeniería, Pontificia Universidad Católica Argentina, Av. Pellegrini 3314, S2002QEO Rosario, Santa Fe, Argentina
[*] Author to whom any correspondence should be addressed.

E-mail: christian.cuadrado@uv.es

Keywords: mode-locking, polarization-maintaining, thulium-doped, fiber laser

Abstract

In this work, we present a passively modelocked all-fiber laser that fully retains polarization with a fundamental repetition rate of 1 GHz. The whole cavity consists of a 106 mm-long highly-Tm-doped polarization-maintaining fiber with a dichroic mirror on one end and a semiconductor saturable absorber mirror on the other. We experimentally characterized the output of this laser, which emits a train of transform-limited light pulses with a temporal width of 520 fs at the central optical wavelength of 1.96 μm. The high stability of this laser was also experimentally verified. Together with this, a detailed theoretical model was developed, confirming the experimental results.

1. Introduction

Over the past few decades, a great deal of research has focused on the creation of high-performance passively modelocked ultrafast lasers with a repetition rate in the range of several hundred MHz to GHz [1–3]. This feature is particularly crucial for many applications, including high-speed optical sampling [4], frequency metrology [5], and optical arbitrary waveform generation [6]. The compact size and inherently high beam quality of all-fiber lasers make them stand out among other solutions. Further, through nonlinear frequency conversion, ultrafast fiber lasers operating at 2 μm have recently been shown to be an effective platform to access the mid/far-infrared spectral region [7], where a high repetition rate is interesting in order to achieve higher average powers. Therefore, it is expected a high demand for 2 μm high repetition-rate fiber lasers. Although harmonic mode-locking is a well-known method for achieving high repetition rates [8], it has the drawback of producing additional noise, such as amplitude variations and temporal disturbances between pulses. Worse still, the repetition rate might alter due to environmental disturbances. On the other hand, fundamentally modelocked fiber lasers with high repetition rate are far better as the noise level is substantially lower and the output pulses have a duration that is precisely determined by the cavity length. Nevertheless, it can be difficult to mode-lock a fiber laser at a repetition rates higher than 200 MHz. Since the cavity is only ∼500 mm long, the active fiber needs to be heavily doped in order to give sufficient gain, especially at repetition rates in excess of 1 GHz [9]. As an example, for optical frequency metrology applications, the required optimal comb line spacing might vary in the range 0.01–100 GHz. However, it is particularly versatile a comb spacing about 1 GHz; because it enables straightforward electrical interface and high-speed acquisition in dual-comb spectroscopy [10] and three-dimensional imaging [11]. Additionally, compared to sources with lower repetition rates, the power per comb line is higher, improving the signal-to-noise ratio [12].

Several high fundamental repetition rates 2 μm modelocked fiber laser sources have recently been presented. Akosman *et al* reported a Tm/Hm-doped laser with a mixed bulk optic/fiber optics configuration [13]. This laser generated transform-limited soliton light pulses with a FWHM of 0.315 ps at a repetition rate of 253 MHz. In the same year, Kuan *et al* presented an all-fiber configuration using a double-cladding thulium-doped fiber (TDF) [14]. In this case, they obtained a pulse train at the fundamental repetition rate of 535 MHz, where each light pulse having a FWHM of 7.9 ps and a 3 dB bandwidth of 0.72 nm. Later, the same team from [13]. Scaled the repetition rate up to the gigahertz regime with the same configuration used before, except by the replacement of the medium gain by a TDF [15]. Therefore, they obtained a train of transform-limited light pulses with a 0.43 ps FWHM at a repetition rate of 1.25 GHz. We could mention also the work of Cheng *et al* [16], where they presented a temperature-controlled cavity emitting at the fundamental repetition rate of 1.6 GHz a train of light pulses whose temporal width estimated from spectral measurements was 0.217 ps. On the other hand, Qiao *et al* demonstrated modelocked emission at two microns of watt-level few-cycle pulses at 1 GHz of fundamental repetition rate, but using multi-stage fiber amplification and extra-cavity nonlinear pulse compression [17]. Even, fundamental repetition rates of 10 GHz have been obtained at two microns with a similar setup [18].

To the best of our knowledge, this is the first study to present a polarization-maintaining (PM) thulium-doped mode-locked fiber laser operating at a fundamental repetition rate of 1 GHz in a laser cavity based entirely on commercially available components. The performance of the full laser was characterized, including a stability analysis. Further, we modeled this laser, confirming the numerical results our experimental measurements.

2. Experimental

In figure 1(a) we show the experimental setup, the PM oscillator consisted of a short Fabry–Perot (FP) resonator that fully preserves polarization. This resonator is pumped by a CW laser emitting at 1561 nm, with a maximum power of 800 mW and a lasing threshold of 47 mW. The pump power entered the FP cavity via a dichroic filter deposited on a fiber ferrule (transmissivity >90% at 1561 nm, reflectivity ∼99% for optical wavelengths higher than 1780 nm), see its transmittance curve T_d in figure 1(b). This fiber ferrule in turn belongs to one extreme of a highly doped (∼7%) PM TDF (PM-TSF-5/125, Panda-Type Tm-Doped optical fiber by Nufern, numerical aperture 0.24, operating wavelength 1900–2100 nm, and 362 dB m^{-1} absorption at 1560 nm). The emission cross section σ_e for a highly-doped TDF can be seen in figure 1(b) [19]. Finally, the FP cavity was closed by facing a SESAM (SAM-1960-30-10 ps-x, BATOP, relaxation time constant $\tau \sim 10$ ps, modulation depth $\Delta R = 18\%$) to a second fiber ferrule attached to the remaining extreme of the PM TDF. The measured reflectance and group delay dispersion (GDD) for the SESAM are shown in figures 1(b) and (c), respectively [20]. The laser output is generated via a PM wavelength division multiplexer situated outside the FP cavity. This multiplexer operates at wavelengths of 1550 nm and 1950 nm, exhibiting an insertion loss of less than 0.6 dB for transmission to the common port at 1950 nm, and less than 0.5 dB for reflection to the common port at 1550 nm. Subsequently, it connects to a PM fiber optic coupler, characterized by a 90/10 splitting ratio, a central wavelength of 1950 nm, and a blocked fast axis. Additionally, a PM optical isolator is incorporated to prevent undesired reflections from entering the cavity, with a central wavelength range of 1950 ± 20 nm, a peak isolation of 28 dB, and an insertion loss of 0.6 dB. Naturally, the anticipated output from this laser is linearly polarized due to the inclusion of a fiber optic coupler blocking the fast axis, see figure 1. On the other hand, since the PM TDF length was 0.106 m, the resonator round-trip length was 0.212 m. The group velocity dispersion (GVD) of the PM TDF and GDD of the SESAM are -20 ps^2 km^{-1} [21] and -600 fs^2, respectively, at 1960 nm. Thus, the total GDD per round-trip within the cavity is—4840 fs^2, i.e., anomalous. A sampling oscilloscope with a bandwidth of 63 GHz (Agilent Infinium DCA-J 86 100 C), a real-time oscilloscope with a bandwidth of 13 GHz (Keysight UXR0134A), fast InGaAs photodetectors with rise/fall timings of less than 28 ps (EOT ET-5000 F), an optical spectrum analyzer with a resolution of 50 pm (Yokogawa AQ6375), and an 32 GHz bandwidth electrical spectrum analyzer with a resolution of 1 Hz (Keysight EXA N9010A) were all used to characterize the laser. Finally, an optical power meter unit was also used to record the average output power over time (Artifex OPM150).

The modelocked operation self-started at a pump power of ∼300 mW (measured at the input of the dichroic mirror), although with some amplitude instabilities. These instabilities diminished when the pump power reached 339 mW. At this pump power level, the laser produces a consistent single-pulse train with a repetition rate of 947 MHz, which aligns perfectly with the anticipated round-trip duration for a FP cavity featuring a round-trip length of 0.212 m, as illustrated in figure 2(a). Conversely, the optical spectrum is depicted in figure 2(b), exhibiting a 3-dB bandwidth of 7 nm, centered on 1960 nm.

Next, the fast photodetectors were connected to an RF spectrum analyzer; figure 3(a) shows the trace measured with a resolution bandwidth of 1 kHz for a wide span covering up to the 5th harmonic. They are

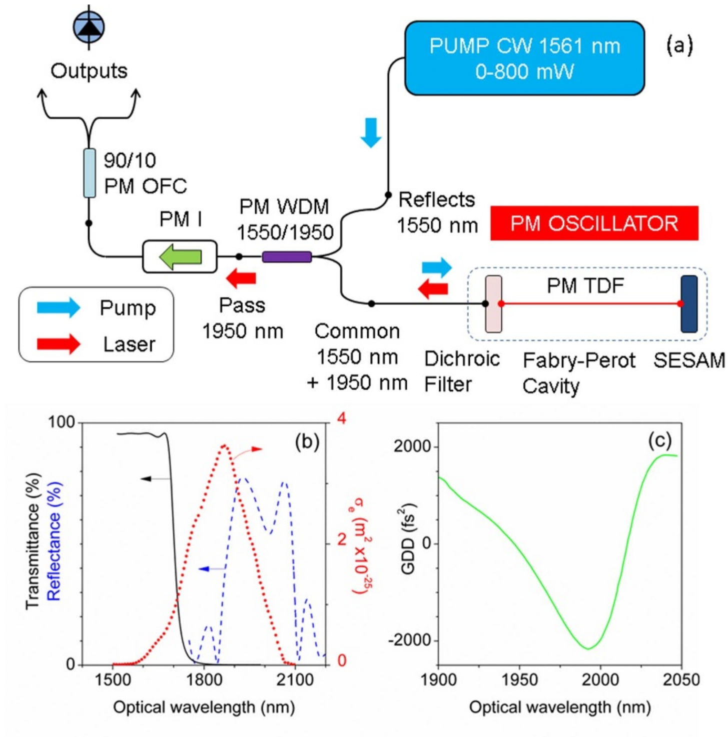

Figure 1. (a) Experimental setup of the PM TDF Fabry–Perot modelocked fiber laser. (b) Left axis: transmittance and reflectance measured for the dichroic filter (solid black curve) and SESAM (dotted blue curve), respectively; right axis: emission cross section σ_e of the TDF (solid red points). (c) GDD of the SESAM.

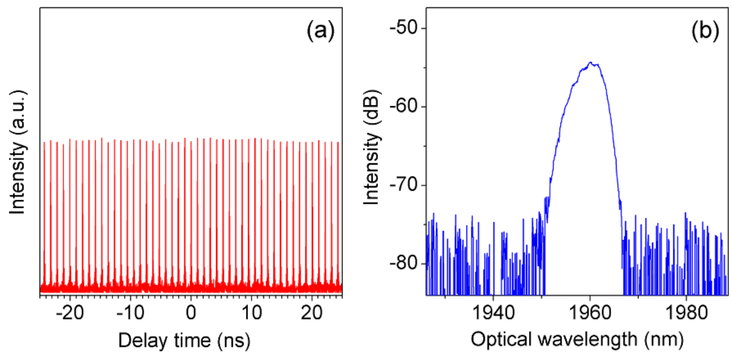

Figure 2. Pulse train operating at a fundamental repetition rate of 1 GHz, along with its associated optical spectrum, (a) and (b), respectively.

equally spaced at 947 MHz, showing a high extinction sideband suppression ratio >50 dB. From the RF spectra, we conclude the emission of this laser is stable, as is evidenced by the absence of low-frequency instabilities. On the other hand, the average output power measured was 15.2 μW, resulting in a slope efficiency of 0.0152 mW/339 mW; i.e. 0.04%. The stability of this laser was also investigated by recording the output average power for continuous running operation. The laser functioned continuously without any external support or oversight, and without regulation of the room temperature, which presented a temperature variation of ∼8 °C during the measurements. Despite these conditions, the laser operated seamlessly, exhibiting only a minor fluctuation in the average output power of merely 2% of standard deviation over a period of 3.5 h, as illustrated in figure 3(b). During the temporal measurements, the pulse width, repetition rate and peak power showed a standard deviation of 2.6%, 0.5% and 3%, respectively. The incorporation of a SESAM as a mode-locker, along with a fully PM cavity, guarantees resilience to temperature fluctuations and mechanical disturbances [22, 23].

Finally, because the light pulse at the output of the oscillator is too short to be measured with our oscilloscope, we chose to estimate it using an autocorrelator. Unfortunately, the energy of the pulse was not high enough to overcome the noise floor. Further, to preserve the original waveform of the pulse profile at

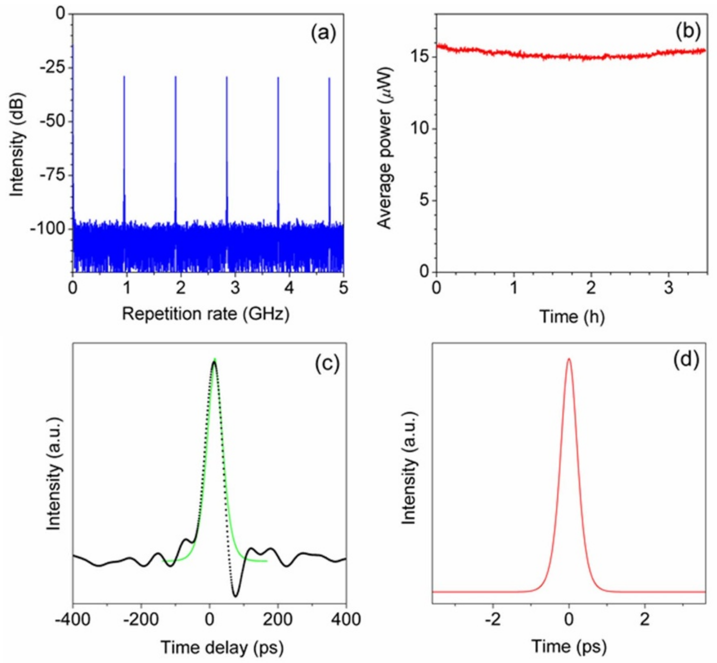

Figure 3. RF spectrum showing up to the 5th harmonic, and measured output power in long range operation, (a) and (b), respectively. (c) Oscilloscope trace measured at the output of the dispersive line (solid scatter points), together with the simulation of a pulse profile dispersed by the same dispersive line (solid green curve). (d) Pulse profile reconstructed at the output of the oscillator.

the output of the oscillator, we avoided the use of optical amplification. As a result, we used another method that involved measuring the pulse broadened under a known dispersion and then recalculating the required pulse width at the input of the dispersive line to match the calculated dispersed profile to the measured one [24]. To accomplish this, we transmitted the pulse train from the oscillator via a 210 m-long optical fiber (Corning LEAF®, numerical aperture 0.14), whose chromatic dispersion at this wavelength had previously been measured by us using an interferometric technique [+34.15 ps/(nm km) at 1961 nm] [25]. We avoided using longer dispersion lines at this power level due to the considerable attenuation present (-11.6 dB km^{-1} at 1961 nm). Figure 3(c) depicts the temporal pulse profile obtained at the output of the 210 m-long dispersive line, with FWHM of 54 ps. In contrast, we simulated the propagation of an unchirped sech^2 light pulses with varying temporal widths for the same dispersive line. Only when the temporal width of the pulse profile at the input of the dispersive line was 0.53 ps could we reasonably fit the measured dispersed light pulse to the simulated dispersed pulse; see figures 3(c) and (d), respectively. It was implicitly assumed a transform-limited pulse because, in this regime, this laser is expected to emit a soliton-like pulse with a minimum time-bandwidth product; i.e., 0.315 for sech^2 pulses [26]. On the other hand, the spectral bandwidth measured at the oscillator output was 7 nm, yielding a time-bandwidth product of 0.29, consistent with our initial assumption.

3. Theory

The generalized scalar nonlinear Schrödinger equation has become a significant mathematical tool for analyzing and simulating the propagation of optical pulses in diverse cavity configurations, including fiber optic systems and laser resonators. This equation builds upon the classical nonlinear Schrödinger equation by incorporating supplementary terms that represent a range of physical phenomena, such as higher-order dispersion, nonlinear interactions, and mechanisms for energy gain and loss [27, 28]:

$$\frac{\partial A}{\partial z} = -\alpha\frac{A}{2} + \int_{-\infty}^{\infty} \frac{g(\omega)}{2}\hat{A}e^{-j\omega t}\mathrm{d}\omega - j\frac{\beta_2}{2}\frac{\partial^2 A}{\partial t^2} + j\gamma|A|^2 A, \tag{1}$$

where $A = A(z, t)$ represents the complex envelope of the optical pulse, t signifies the local pulse time as observed in a reference frame that moves at the same velocity as the signal. The variable z indicates the distance of propagation, while α denotes the linear loss. Additionally, β_2 refers to the GVD, and γ represents the nonlinear coefficient. The circumflex accent over a function corresponds to the Fourier transform of that

Table 1. Parameters used in the model of the PM Tm-doped Fabry–Perot modelocked fiber laser.

	Parameter	Value	Units
Dichroic mirror	The spectral dependence for the dichroic reflectance was taken from figure 1(b)		
Gain medium	g_0	64	m^{-1}
	L	0.106	m
	β_{20}	–20	ps^2/km
	γ	0.8×10^{-3}	$W^{-1}m^{-1}$
	E_s	2	pJ
	The spectral dependence for $g_0(\omega)$ follows σ_e shown in figure 1(b)		
SESAM	ΔR	18	%
	Φ_{sat} [a]	0.65	$J\,m^{-2}$
	A_{sat} [b]	23.76	μm^2
	τ	10	ps
	The spectral dependence for reflectance and GDD follows figures 1(b) and (c), respectively		

[a] Saturation fluence,
[b] Saturation area.

function ($\Im$); i.e. $\hat{A} = \Im(A)$, and $g(\omega)$ is the gain coefficient. The baseband angular frequency, ω, is defined as $\omega = \omega_{opt}$—ω_0, with ω_{opt} being the optical angular frequency and ω_0 the carrier angular frequency. The gain saturation, on the other hand, was considered as:

$$g(\omega) = \frac{g_0(\omega)}{1 + \frac{\int |A|^2 dt}{E_S}}. \tag{2}$$

The gain coefficient for small signals, denoted as $g_0(\omega)$, is associated with the doping concentration and exhibits a spectral dependence illustrated in figure 1(b), following the emission cross section σ_e; while E_S is the saturation energy, which is typically related to pumping strength. It has been demonstrated that raising the pump power simultaneously raises g_0 and E_S; nevertheless, in most cases, maintaining g_0 at a fixed value and adjusting only E_S is adequate to capture the whole dynamic trend [29]. The gain resulting from an active medium is represented by equation 2, which is independent of time since it has a significantly longer recovery time than the cavity round-trip time [30]. In contrast, the time-dependent absorption of the SESAM can be modeled as a system with two-levels, in which photons from the optical beam excites electrons in the valence band of the semiconductor absorber material from their ground state to the conduction band [31]. Mathematically, the action of the SESAM was modeled in two steps. First, the nonlinear part of the saturation loss is applied to the temporal complex envelope of the pulse profile by using the saturable absorption, which in turn is a function of the intensity of the pulse itself. Second, the linear part of the saturation loss plus the delay dispersion of the SESAM are applied on the complex envelope of the Fourier transform of the pulse profile. Therefore, the temporal waveform performs first a saturation action on the reflectivity promoted by its intensity (nonlinear action), which is then followed by a filtering action in the spectral domain via the reflectance dependence on wavelength shown before in figure 1(b) (linear action). Further information regarding the methodology for modeling the SESAM is available in the existing literature [32, 33]. Table 1 shows the parameters used in the calculation, which were chosen based on the available data sheets of the components we effectively used in our setup, or in equivalent components when comprehensive data sheets were unavailable. A single round-trip corresponds to a propagation of the optical field through all components within the resonator back and forth following equation 1. After each round-trip, the spectrum of the signal intensity is multiplied by the dichroic filter wavelength dependent reflectance R_d to account for dichroic action before returning to the program, with $R_d = 1 - T_d$, and T_d previously shown in figure 1(b). The numerical simulations were running with 2^{14} uniformly distributed points across a 500 ps time window using the split-step Fourier transform approach [20]. Random noise was employed as the initial field, consisting of one photon per frequency channel. This initial field was used as input to the medium gain in the first iteration, with the output being obtained through the dichroic filter in the last iteration. The routine was coded using the well-known mathematical software MATLAB.

We show in figures 4(a) and (b) the simulated evolution of the temporal and spectral profiles from noise as a function of the round-trip number. The optical field inside the cavity evolves in a sequence of multiple

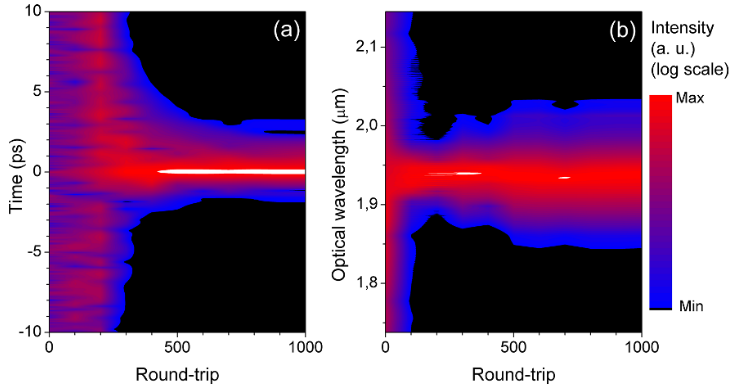

Figure 4. Simulation of the build-up of the emission from noise in the temporal (a), and spectral (b), domains as a function of the round-trip number.

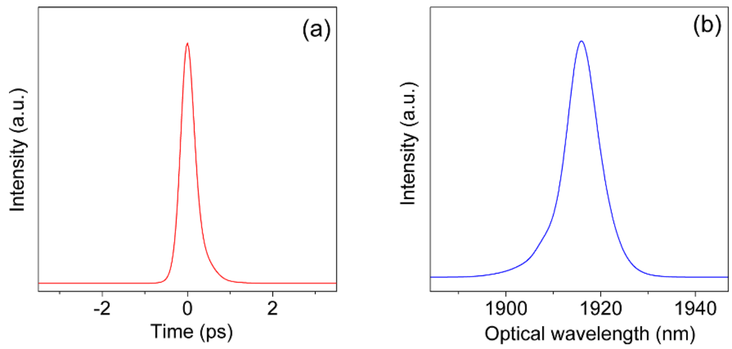

Figure 5. Temporal waveform and optical spectrum for the thousandth round-trip, (a) and (b), respectively.

pulses per round-trip from noise, up to round-trip ~300, when it is distinguished as a single pulse. However, both its temporal profile and its spectrum are not sufficiently defined at this stage yet. After that, one must wait until round-trip >700 in order to reach a steady-state regime where the pulse profile takes on its final shape with a distinct temporal and spectral profile. In this case, the saturation energy E_s is the adjust variable; it serves the same purpose as pump power in the setup and, to replicate the experimental results, it should be chosen to be approximately 2 pJ, see table 1. While a significantly higher value of E_s generates multiple pulses per roundtrip, a significantly lower value of E_s fails to produce clean light pulses and instead produces a noise output.

Finally, figure 5(a) depicts the time domain waveform in detail for the thousand round-trip; the pulse has an FWHM of 0.5 ps. The obtained numerical spectrum centered at 1916 nm, has a FWHM of 7.8 nm, and it is shown in figure 5(b). The time-bandwidth product is 0.315 confirming both the transform-limited and sech^2 profile nature of the emission. The spectrum does not show sidebands, which is consistent with the experimental measurements. The numerical values in the temporal and spectral domains agree reasonably well with the experimental values presented except by the spectral shift in the emission (from the experimentally measured 1961 nm to the calculated 1916 nm). We believe this mismatch could be due to the unknowing of $g_0(\omega)$, where we used another provided in the literature for a similar fiber [14].

It is noteworthy to take advantage of this numerical model to investigate how the alteration of the parameters characterizing this configuration influences the output pulse profile, with the objective of optimizing its performance for future advancements. We start by the SESAM first, as its modulation depth ΔR is varied, the pulse characteristics remain predominantly stable, contingent upon the adjustment of the number of roundtrips required to reach a steady-state. For example, when $\Delta R = 1.8\%$, which is one order of magnitude lower than the value indicated in table 1, more than ten thousand roundtrips are necessary to achieve a steady state, indicating a substantial increase in the number of required roundtrips. Furthermore, when the relaxation time constant τ is decreased to 1 ps from its original value of 10 ps (see table 1), the trailing edge of the pulse profile becomes much more symmetrical in relation to the leading edge, closely approximating a true sech^2 profile, along with a slight temporal narrowing of approximately 10%. Conversely, a one order of magnitude increment in the relaxation time constant; i.e. $\tau = 100$ ps, results in a significant elongation of the trailing edge, which slightly broadens the overall pulse profile. Of course when τ approaches the roundtrip time, it becomes impossible to achieve a steady-state regime. On the other hand, the decrease in saturation fluence Φ_{sat}, primarily results in a diminished saturation energy required to attain a steady-state mode-locking condition, without yielding any other significant effects. As a result, using a SESAM with differing properties is unlikely to result in considerable stretching of the output pulse width in this setup. To the best of our knowledge, the SESAM we used, based on GaAs technology, is not commercially available at two microns with τ <10 ps. However, SESAMs based on other technologies could be considered, such as GaSb; whose reported values for τ are an order of magnitude lower near the mid-IR region [34]. The dichroic reflectivity was the only other parameter that could be adjusted within the cavity. However, as expected, changes to this parameter have little effect on the pulse profile, except for the peak power, which slightly drops as the reflectivity lowers. As a result, we may infer that the experimentally reported values are within the best that could be obtained with this arrangement. Finally, we numerically tried different combinations for intracavity dispersion, and we found that this setup could work in the normal non-solitonic dispersion regime, either by adding a short piece of normal dispersion fiber or eventually by SESAM dispersion engineering. In this case the pulse width is approximately equal to our experimental measurements but non-bandwidth limited, i.e., chirped. In this way, shorter light pulses could be obtained by common dispersion compression techniques out of the cavity.

4. Conclusions

In summary, we have demonstrated the viability of short FP fiber lasers emitting at 2 μm with a 1 GHz repetition rate in a full polarization-preserving cavity. Furthermore, the robust stability exhibited by this laser has been tested and confirmed experimentally. To complement our experimental observations, a comprehensive theoretical framework was formulated, with numerical simulations effectively corroborating the experimental measurements. The strong agreement between our theoretical predictions and experimental data gives us confidence in our developed theoretical model to predict the effects on the pulse profile of those elements in the cavity that are more or less easily modifiable, in particular the relaxation time constant, saturation fluence, and modulation depth of the SESAM, plus the reflectivity of the dichroic filter. However, the numerical results shown that none of these factors were significant enough to substantially reduce the pulse width we experimentally measured, despite the fact that it was evident that each of them directly affected the emission. As a future step, we are currently working on an extension of this study in which we carefully investigate both experimentally and theoretically how the emission changes as the cavity is gradually shortened from a fundamental repetition rate of 100 MHz to 1 GHz Further miniaturization in order to achieve higher repetition rates will benefit from improvements of the TDF itself, in order to provide higher gain.

Data availability statement

All data that support the findings of this study are included within the article (and any supplementary files).

Acknowledgment

This work was supported in part by the European Union, project IPN-Bio (Ref.: H2020-MSCA-RISE-2019-872049), and by the Generalitat Valenciana of Spain (Ref.: CIPROM/2022/30).

Conflict of interest

The authors declare no conflicts of interest.

ORCID iDs

C Cuadrado-Laborde https://orcid.org/0000-0003-1620-6751
P Pérez-Millán https://orcid.org/0000-0002-5872-8278
A Díez-Cremades https://orcid.org/0000-0003-1045-0411
J L Cruz https://orcid.org/0000-0002-4360-9989
E Silvestre https://orcid.org/0000-0002-4092-8597
M V Andrés https://orcid.org/0000-0003-0103-8644

References

[1] Zhang J, Kong Z, Liu Y, Wang A and Zhang Z 2016 *Photon. Res.* **4** 27
[2] Chen X, Lin W, Wang W, Guan X, Wen X, Qiao T, Wei X and Yang Z 2021 *Opt. Lett.* **46** 1872
[3] Muñoz-Marco H, Abreu-Afonso J, Sardiello G and Pérez-Millán P 2020 *Appl. Opt.* **59** 6817
[4] Bartels A, Cerna R, Kistner C, Thoma A, Hudert F, Janke C and Dekorsy T 2007 *Rev. Sci. Instrum.* **78** 035107
[5] Schibli T R, Minoshima K, Hong F-L, Inaba H, Onae A, Matsumoto H, Hartl I and Fermann M E 2004 *Opt. Lett.* **29** 2467
[6] Cundiff S T and Weiner A M 2010 *Nat. Photon.* **4** 760
[7] Smolski V O *et al* 2016 *Opt. Lett.* **41** 1388
[8] Luo Z-C, Liu M, Liu H, Zheng X-W, Luo A-P, Zhao C-J, Zhang H, Wen S-C and Xu W-C 2013 *Opt. Lett.* **38** 5212
[9] Chang G and Wei Z 2020 *iScience* **23** 101101
[10] Phillips C R, Willenberg B, Nussbaum-Lapping A, Callegari F, Camenzind S L, Pupeikis J and Keller U 2023 *Opt. Express* **31** 7103
[11] Kurata S, Ishii H, Terada K, Morito T, Tian H, Kato T and Minoshima K 2022 *Opt. Contin.* **1** 2374
[12] Müller M, Hamrouni M, Komagata K N, Parriaux A, Wittwer V J and Südmeyer T 2023 *Opt. Express* **31** 44823
[13] Akosman A E and Sander M Y 2016 *IEEE Photonics Technol. Lett.* **28** 1878
[14] Kuan P-W, Li K, Zhang L, Li X, Yu C, Feng G and Hu L 2016 *IEEE Photonics Technol. Lett.* **28** 1525
[15] Zeng J, Akosman A E and Sander M Y 2018 *Opt. Express* **26** 24687
[16] Cheng H, Wang W, Zhou Y, Qiao T, Lin W, Guo Y, Xu S and Yang Z 2018 *Opt. Express* **26** 16411
[17] Qiao T, Cheng H, Wen X, Wang W, Lin W, Zhou Y, Guo Y, Liu Y and Yang Z 2019 *Opt. Lett.* **44** 6001
[18] Liang Z, Lin W, Wu J and Chen X 2022 *Opt. Lett.* **47** 1867
[19] Lee Y-W, Chien H-W, Cho C-H, Chen J-Z, Chang J-S and Jiang S 2013 *Fibers* **1** 82–92
[20] BATOP GmbH 2024 *SAM - 2000 nm* (available at: www.batop.de/products/saturable-absorber/saturable-absorber-mirror/saturable-absorber-mirror-2000nm.html)(Accessed 1 October 2024)
[21] Sotor J, Bogusławski J, Martynkien T, Mergo P, Krajewska A, Przewłoka A, Strupiński W and Soboń G 2017 *Opt. Lett.* **42** 1592
[22] Cuadrado-Laborde C *et al* 2023 *Appl. Sci.* **13** 1981
[23] Cuadrado-Laborde C, Cruz J L, Díez A and Andrés M V 2022 *IEEE Photon. J.* **14** 1539005
[24] Cuadrado-Laborde C, Brotons-Gisbert M, Serafino G, Bogoni A, Pérez-Millán P and Andrés M V 2014 *Appl. Phys.* B **117** 1173
[25] Hlubina P 2001 *Opt. Commun.* **193** 1–7
[26] Siegman A E 1986 *Lasers* (University Science Books)
[27] Agrawal G P 2007 *Nonlinear Fiber Optics* 4th edn (Academic)
[28] Cuadrado-Laborde C, Tendela L, Silvestre E, Díez A, Cruz J L and Andrés M V 2024 *Chaos Soliton Fractals* **13** 100114
[29] Zhang X *et al* 2018 *IEEE J. Sel. Top. Quant.* **24** 1101309
[30] Agrawal G P 2007 *Applications of Nonlinear Fiber Optics* 2nd edn (Academic)
[31] BATOP GmbH SAM - Saturable Absorber Mirror (available at: www.batop.de/information/SAM_infos.html) (Accessed 1 October 2024)
[32] Haiml M, Grange R and Keller U 2004 *Appl. Phys.* B **79** 331
[33] Schibli T, Thoen E, Kärtner F and Ippen E P 2000 *Appl. Phys.* B **70** S41
[34] Normani S *et al* 2024 *Opt. Express* **32** 15106